12B.12 THREE-DIMENSIONAL GRIDDING AND MOSAIC OF REFLECTIVITIES FROM MULTIPLE WSR-88D RADARS

Jian Zhang[1], Jonathan J. Gourley[1], Ken Howard[2], Bob Maddox[1]
[1]Cooperative Institute for Mesoscale Meteorological Studies, Norman, OK
[2]NOAA/National Severe Storms Laboratory, Norman, OK

1. INTRODUCTION

The deployment of the United States NEXRAD (NWS's NEXt generation RADar, the NEXRAD or WSR-88D) network has provided weather forecasters an important tool in the monitoring of severe weather and for issuance of storm warnings. The current operational radar algorithms are based on single radar and are applied in polar coordinates. However, most forecast offices and regional aviation control centers monitor weather and storms over a geographical domain that encompasses several radar umbrellas. Further, the life cycle of an individual storm may be sampled by two or more radars requiring additional radars for better monitoring of storm characteristics and evolution.

The creation of a 3D radar mosaic would allow users and algorithm developers the benefit to use and develop a wide variety of products and displays that more fully depicts the evolution and lifecycle of storms. Examples include more physically realistic horizontal or vertical cross-sections. Single radar algorithms could be expanded to utilize data from multiple radars and other environmental data to more accurately determine storm attributes. Gridded radar data can also be easily combined with information from other data sources such as satellite data, model analyses or forecast fields increasing its value in the overall forecast and warning process. Regional rainfall maps using multisensor approaches are examples of such an application.

Gridding radar data is challenging due to 1) the conical geometry of radar sampling and 2) the large volume of radar data sets. The distribution of radar data is non-uniform in space, with high resolution in the radial direction and low resolution in azimuthal and elevational directions, especially at far ranges.

Corresponding author address: Jian Zhang, NSSL, 1313 Halley Circle, Norman, OK 73069.
Email: jzhang@nssl.noaa.gov

Figure 1.1 shows radar data distributions on a x-z plane in Volume Coverage Pattern (VCP) 21. Near radar, the centers of data bins are spaced by about 1 km, while at far range they are spaced as much as 100 km horizontally and 5 km vertically. This non-uniformity makes the choice of an interpolation scheme and associated filter nontrivial. Trapp and Doswell (2000) tested nearest neighbor, a Barnes-type, and Cressman-type interpolation schemes. Their results show that a nearest neighbor scheme gives the smallest root-mean-square (RMS) errors, but the spatial scales of error fields are non-uniform. A strong Barnes filter based on the poorest resolution in a reflectivity field results in a uniformly scaled error field, but significant high-resolution information in the observations is lost. This is not a desirable feature for monitoring severe storms by observation or by the use of an algorithmic procedure.

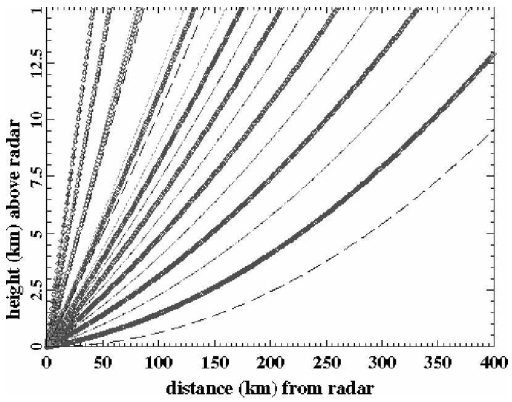

Fig. 1.1 Radar data distributions on a x-z plane in VCP 21. The circles represent the centers of radar bins; the dashed lines indicate the bottom of radar beams, and the dotted lines the top of radar beams. Note that the circles are overlapped on the top of each other at the lower elevation angles.

In this study, we choose an adaptive Barnes-type scheme (Askelson et al., 2000) for interpolating radar data onto a Cartesian grid. This scheme is designed for retaining high-resolution information in the original radar observations while filtering small-scale noise. In

comparison to a uniform Barnes scheme, the adaptive Barnes scheme results in smaller errors in the interpolated fields, especially in regions near radar. Errors in analyzed reflectivity fields must be minimized when producing scalar fields such as precipitation rates and vertically integrated liquid (VIL).

2. CONICAL TO CARTESIAN TRANSFORMATION

The weighting function of the adaptive Barnes filter is defined as:

$$w_{i,k} = \exp\left[-\frac{(r_k - r_i)^2}{\kappa_r} - \frac{(\phi_k - \phi_i)^2}{\kappa_\phi} - \frac{(\theta_k - \theta_i)^2}{\kappa_\theta}\right] \quad (2.1)$$

where, r_i, φ_i, θ_i are range, azimuth, and elevation of the i^{th} grid point; r_k, φ_k, θ_k are range, azimuth, and elevation of the center of k^{th} reflectivity observation bin in the influence region* of the i^{th} grid point; κ_r, κ_ϕ, κ_θ are Barnes smoothing factors in the radial (r-), azimuthal (ϕ-), and elevational (θ-) directions, and $w_{i,k}$ is weight given to the k^{th} reflectivity observation at the i^{th} grid point.

The interpolated value at the i^{th} grid point is calculated by:

$$f_i^a = \frac{\sum_{k=1}^{nobs} w_{i,k} f_k^o}{\sum_{k=1}^{nobs} w_{i,k}} \quad (2.2)$$

Here, f_i^a represents the interpolated reflectivity at the i^{th} grid point, f_k^o is the observed reflectivity at the k^{th} radar bin, and "nobs" represents the number of radar bins within the influence region of the i^{th} grid point.

In the adaptive Barnes scheme, there is approximately the same number of data points within the influence region of each grid point. The algorithm is computationally efficient since the number of data points is small when the filter is designed to retain high-resolution information in the raw data. On the other hand, a uniform Barnes scheme with large smoothing factors is computationally expensive because the number of data points within an influence region becomes very large at close ranges (Fig.1.1).

*** The influence region is a volume that is centered at a grid point and bounded by constant radial, azimuth and elevation distances (R_{i_r}, R_{i_ϕ}, and R_{i_θ}) away from the grid point. R_{i_r}, R_{i_ϕ}, and R_{i_θ} are the distances where the interpolation weight become equal or less than a lower threshold value.**

3. GAP-FILLING

There are data gaps between the higher tilts in VCP 21 (Fig. 1.1) and VCP 11 (not shown) due to large elevation angle spacings. To fill in the gaps, one option is to increase the smoothing factor κ_θ in the weighting function (Eqn.[2.1]) so that the radius of influence becomes large at higher elevations. However, we found that this solution results in arc-shaped discontinuities or concentric circles in the interpolated field when there is horizontally homogeneous echo having strong vertical gradients (e.g., stratiform precipitation). Fig. 3.1 shows a vertical cross-section of reflectivity with a melting layer between 2-4 km. Fig. 3.2a shows a horizontal cross-section of an interpolated reflectivity field at 3.5 km. The high reflectivity arcs seen northwest of the radar are associated with places where the melting layer intercepts the center of radar beams, while the intervening gaps correspond to locations where the bright band intercepts vertical scanning gaps. For grid points in these intervening gaps, the interpolated values are derived from reflectivity in radar bins much higher above or much lower below. This height uncertainty problem has been discussed in previous studies (Howard et al., 1997, Maddox et al., 1999, and Brown et al., 2000). To alleviate this problem, we used an alternate gap-filling scheme in which a horizontal interpolation is performed between the gaps. Fig. 3.2b shows the same horizontal section after the horizontal gap-filling scheme was employed. The discontinuities have been effectively removed.

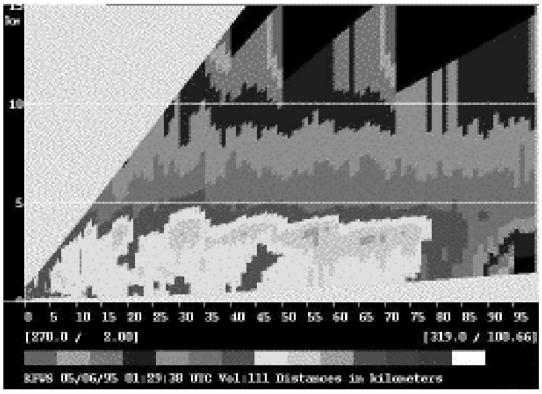

Fig. 3.1 A vertical cross-section of the reflectivity observed by KFWS at 1:30 UTC, May 6, 1995. The cross-section was taken along a line from "A" to "B" in Fig. 3.2a.

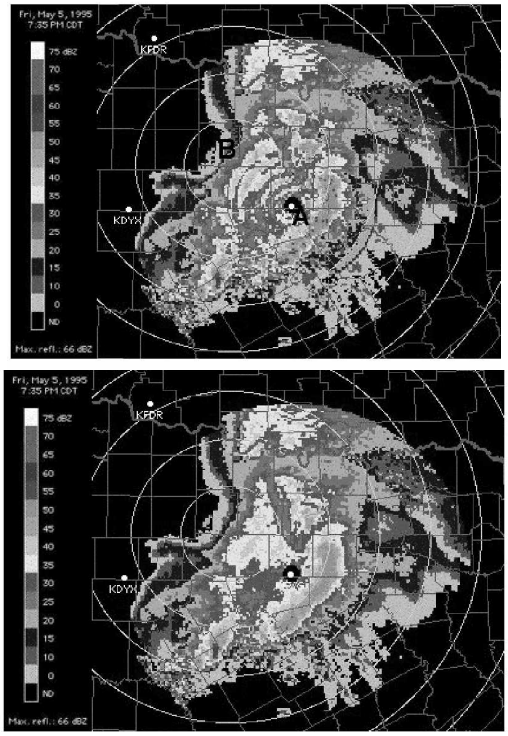

Fig. 3.2 Horizontal sections of the interpolated reflectivity at 3.5 km (msl) before (panel a) and after (panel b) a horizontal gap-filling scheme was employed.

4. MOSAIC

The polar-to-Cartesian transformation is performed for each individual radar's volume scan. The remapped reflectivity fields from different radars, which are valid within a given time window (e.g., 10 minutes), are then mosaicked to produce one 3D reflectivity grid using a Cressman type scheme. The mosaic equation is:

$$f_i^m = \frac{\sum_{j=1}^{nrad} w_{i,j} f_{i,j}^a}{\sum_{j=1}^{nrad} w_{i,j}} \qquad (4.1)$$

where $f_{i,j}^a$ represents the interpolated value at the i^{th} grid point from the j^{th} radar, f_j^m is the mosaicked reflectivity value at the grid point, $w_{i,j}$ is the weight given to $f_{i,j}^a$. The weight is determined by:

$$w_{i,j} = \frac{R_i^2 - d_{i,j}^2}{R_i^2 + d_{i,j}^2} \qquad (4.2)$$

Here R_i is the influence radius of radar, which is set to 300 km in our scheme, and $d_{i,j}$ is the distance between the j^{th} radar and the i^{th} grid point.

Fig. 4.1 shows examples of single radar composite reflectivities from KFWS, KGRK and KTLX, and a mosaicked composite reflectivity. The data are from the Ft. Worth, TX, USA hailstorm case that occurred on May 5-6, 1995. The mosaicked reflectivity provides a more comprehensive depiction of the storm structures and could be more useful for making weather-related decisions than single radar products.

5. SUMMARY

A multiple radar reflectivity mosaic scheme has been developed, tested, and employed in real-time operations. An adaptive, Barnes-type filter is used to transform radar reflectivity from their native conical coordinates to Cartesian grids. A Cressman-type scheme is then used for mosaicking multiple radar fields. The advantages of the scheme include its computational efficiency and the retention of high-resolution meteorological information. The multiple radar reflectivity mosaic has been tested in several applications including a real-time regional reflectivity display, an aviation control display and a radar climatological study.

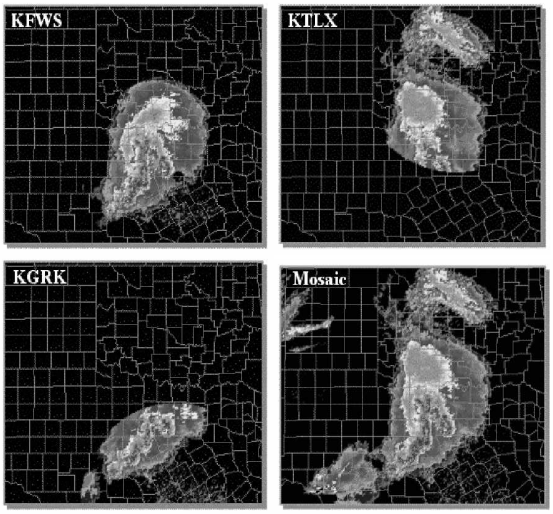

Fig. 4.1 Composite reflectivities from KFWS, KTLX, KGRK radars and from a 3D reflectivity mosaic using 7 radars (the aforementioned 3 plus KAMA, KLBB and KEMX). The images were valid at 2330 UTC on May 5, 1995.

6. RERENCES

Available upon request.